DEM analysis of the onset of flow deformation of sands: linking monotonic and cyclic undrained behaviours

DEM analysis of the onset of flow deformation of sands: linking monotonic and cyclic undrained behaviours

Xin Huang[1,2*], Chung-yee Kwok[3], Kevin J Hanley[4], Zixin Zhang[1,2]

[1] Department of Geotechnical Engineering, Tongji University, 1239 Siping Road, Shanghai 200092, China

[2] Key Laboratory of Geotechnical Engineering, Ministry of Education, 1239 Siping Road, Shanghai 200092, China

[3] Department of Civil Engineering, The University of Hong Kong, Pokfulam Road, Hong Kong, China

[4] Institute for Infrastructure and Environment, School of Engineering, The University of Edinburgh, Edinburgh EH9 3JL, United Kingdom

Abstract

This study explores the link between the monotonic and cyclic undrained behaviour of sands using the discrete element method (DEM). It is shown that DEM can effectively capture the flow deformation of sands sheared under both monotonic and cyclic undrained loading conditions. When subjected to cyclic shearing, flow-type failure is observed for a loose sample, while cyclic mobility is observed for a dense sample. A strong correlation between the monotonic and cyclic loading behaviour that has been revealed experimentally is also confirmed in DEM simulations: a) flow deformation occurs in the compressive loading direction when the cyclic stress path intersects the monotonic compression stress path prior to the monotonic extension stress path, and vice versa; b) the onset of flow deformation in *q-p'* space is located in the zone bounded by the critical state line and the instability line determined from monotonic simulations. Hill's condition of instability is shown to be effective to describe the onset of flow failure. Micro-mechanical analyses reveal that flow deformation is initiated when the index of redundancy excluding floating particles drops to below 1.0 under both monotonic and cyclic loading conditions. Flow deformation induced by either monotonic or cyclic loading is characterized by abrupt change of structural fabric which is highly anisotropic. The reason why the dense sample

[*] Corresponding author: Email: xhuang@tongji.edu.cn; Phone: +86 (0)21 6598 4551; Fax: +86 (0)21 6598 4551

dilated during monotonic loading but showed cyclic mobility (temporary liquefaction) during cyclic loading is attributed to the repeating reversal of loading direction, which leads to the periodic change of microstructure.

Keywords: Liquefaction; flow deformation; stability; monotonic; cyclic; fabric

1 Introduction

It has been widely documented in the literature that sands, when sheared in an undrained state, may liquefy under both monotonic and cyclic loading conditions [1-6]. The mechanism triggering flow failure has been carefully considered by geotechnical researchers over the past decades. It is now commonly accepted that flow deformation is initiated when the instability state is reached, post which the effective stress decreases quickly and flow deformation is developed fastly to static liquefaction (q=p'=0). However, different opinions prevail on the initiation of flow deformation induced by cyclic loading. Vaid and Chern [7] observed in their triaxial tests on loose sands that flow deformation is triggered when the stress path reaches the critical stress ratio (CSR) line which is commonly termed the instability line (ISL) in monotonic undrained tests [4,8]. The ISL connects the peak and the origin in the deviatoric stress (q)-mean effective stress (p') plane. Based on cyclic simple shear test data, Alarcon-Guzman et al. [9] proposed that flow deformation occurs when the effective cyclic loading stress path intersects the effective monotonic stress path, after which the two stress paths will essentially be the same. Hyodo et al. [3] suggested that flow deformation is initiated when the peak of the cyclic loading stress path intersects the phase transformation (PT) line obtained in the monotonic undrained test and lies in the unstable region bounded by the CSR line and the critical state (CS) line. The experimental data of Yang and Sze [5-6] supported Vaid and Chern [7]. Yang and Sze [6] further pointed out that if the CSR line obtained in monotonic triaxial compression tests is reached by the cyclic stress path prior to that obtained in triaxial extension tests, flow deformation will be compressive; otherwise, flow deformation will be extensive. Despite discrepancies between explanations for the onset of cyclic flow failure, it is generally agreed that the static and cyclic responses of sands are interrelated. For example, Andrade et al. [10] proposed that the static and cyclic liquefaction can be unified by the concept of loss of controllability. Mital and Andrade [11] defined a flow liquefaction potential to explain the origin of liquefaction for loose sands and the origin of cyclic liquefaction for dense sands.

The discrete element method (DEM) [12] has been widely adopted by geotechnical community to investigate the mechanical behaviour of granular materials subjected to various loading conditions [13]. Furthermore, the particle-scale information has been commonly exploited to explore the fundamental mechanisms underlying the macro-scale phenomena. DEM has also been employed to explore the

cyclic liquefaction behaviour of sands. Ng and Dobry [14] were amongst the earliest researchers to use DEM to investigate the undrained cyclic loading behaviour of sands. Sitharam [15] conducted comprehensive 2D DEM simulations to investigate the microstructure evolution of granular materials during undrained cyclic loading considering different influential factors. Kuhn et al. [16] performed undrained cyclic shearing simulations by inputting seismic shearing pulses with non-uniform amplitudes. Xu et al. [17] carried out a series of 3D constant-volume cyclic triaxial tests to link the liquefaction resistance to shear wave velocity. Wang and Wei [18] quantified the particle-void arrangement of granular soils in cyclic mobility and post-liquefaction stages based on 2D DEM simulations. Wang et al. [19] proposed a new micro-scale parameter, mean neighbouring particle distance (MNPD), to describe the development of shear strain post liquefaction. Despite these aforementioned applications of DEM to investigate the cyclic behaviour of sands, the link between the monotonic and cyclic loading behaviours of sands has not yet been discussed. Furthermore, flow-type failure and cyclic mobility were not considered separately in previous studies.

In this study, a series of monotonic and cyclic constant-volume triaxial simulations are performed on DEM samples with different initial void ratios. Different cyclic deviatoric stress amplitudes are applied during cyclic loading. The condition of onset of flow deformation was discussed by linking the cyclic responses with the monotonic responses from both macro- and micro-mechanical perspectives. The different behaviour of sands subjected to monotonic and cyclic loading were explored through micro-mechanical analyses.

2 Overview of DEM simulations

DEM simulations were performed using the PFC^{3D} software [20]. The grading curve of Toyoura sand was approximated in the DEM simulations (Fig. 1). Particles with a diameter below 0.1156 *mm* were ignored because their contribution to the overall mass-based particle size distribution (PSD) is negligible. A simplified Hertz-Mindlin contact model was adopted with a particle shear modulus of 29 GPa and Poisson's ratio of 0.12, which are in the ranges of the properties of quartz [21]. Gravitational force was neglected. A local damping coefficient of 0.1 was used throughout the simulations. A small amount of damping force is needed to delay the occurrence of flow failure and avoid obvious

oscillation in stress-strain responses post flow failure. 19,449 non-contacting spherical particles were created at half of their target diameters within a cylindrical space enclosed by two frictionless flat rigid walls on the top and bottom, and a frictionless cylindrical rigid wall in the circumferential direction. The particles were then expanded to their target sizes and allowed to equilibrate. The assembly was then subjected to isotropic compression under a confining pressure of 500 kPa. Different inter-particle friction coefficients (μ) were used to obtain samples with different initial void ratios. After isotropic compression, μ was set to be 0.5 and the samples were again equilibrated. In the next stage, both monotonic and cyclic constant-volume triaxial simulations were performed to simulate the monotonic and cyclic undrained triaxial tests, respectively. During the cyclic loading simulations, the positions of the rigid walls were adjusted continuously so that the deviatoric stress q ($= \sigma'_1 - \sigma'_3$) followed a sinusoidal form (Eq. 1) while the sample volume remained constant.

$$q = q_{cyc}\sin(\omega t) \tag{1}$$

in which q_{cyc} is the cyclic deviatoric stress, ω is the cyclic loading angular frequency, and t is the running time. A parametric study revealed that when ω is below 10π *rad/s*, the simulation results are not obviously sensitive to the strain rate. Therefore, a ω value of 10π *rad/s* was used in all the simulations, which corresponds to a cyclic loading period T of 0.2s.

Two series of cyclic loading simulations were carried out. In the first series of simulations (C1), constant-volume cyclic loading simulations were performed on a dense sample with a void ratio e_0 = 0.658 and $\sigma'_{3,0}$ = 500 kPa. Three cyclic deviatoric stress amplitudes (q_{cyc} = 200 kPa, 300 kPa and 400 kPa) were applied during cyclic loading. These cyclic deviatoric stress amplitudes correspond to cyclic stress ratios ($CSR = q_{cyc}/2/\sigma'_{3,0}$) of 0.2, 0.3 and 0.4. The second series (C2) comprises four simulations on loose samples, each of which has the same initial state (e_0=0.692, $\sigma'_{3,0}$ = 500 kPa) but is subjected to constant-volume cyclic shearing with different cyclic deviatoric stress amplitudes (q_{cyc} = 150 kPa, 180 kPa, 200 kPa and 300 kPa) corresponding to CSR of 0.15, 0.18, 0.2 and 0.3. These q_{cyc} values were selected to yield flow deformation within affordable computation costs. The details of the cyclic simulations are given in Table 1. Furthermore, to establish a link between the cyclic and monotonic

responses, both strain-controlled monotonic compression and extension simulations were carried out with a strain rate of $1s^{-1}$ on the two samples.

Table 1 Simulation details of constant-volume cyclic loading

	ID	e_0	$\sigma_{3,0}$ (kPa)	q_{cyc} (kPa)	*CSR:* $q_{cyc}/2/p'_0$	μ during isotropic compression	Number of loading cycles to initial flow deformation
C1	①	0.658	500	200	0.2	0.25	12.5
	②	0.658	500	300	0.3	0.25	1.52
	③	0.658	500	400	0.4	0.25	1.01
C2	①	0.692	500	150	0.15	0.30	15.72
	②	0.692	500	180	0.18	0.30	4.15
	③	0.692	500	200	0.2	0.30	2.06
	④	0.692	500	300	0.3	0.30	0.15

3 Simulation Results

3.1 Stress-strain Responses

3.1.1 Monotonic loading simulations

Figure 2 shows the stress-strain behaviour of the loose sample when sheared under constant-volume monotonic loading conditions. As shown in Figure 2(a), in both compression and extension cases, the magnitude of deviatoric stress reaches a peak value and then drops sharply to zero, i.e., complete liquefaction occurs. The inter-particle friction we applied during isotropic compression is smaller than the final value we used during shearing. As noted by Bernhardt et al. [22], this will lead to almost no contact sliding at the beginning of shearing. Therefore, the response at the initial stage of loading is much stiffer and more dilative than that of a real soil. The peak state marks the onset of flow liquefaction and is termed the instability state [4,23-24]. The stress paths in q-p' space are presented in Figure 2(b). The instability lines which connect the origin and the instability states under both compression and extension loading conditions are overlaid in Figure 2(b), and are denoted as ISL-C and ISL-E respectively.

For the dense sample, as Figure 3 shows, the stress-strain responses are persistently dilative. The deviatoric stress increases continuously until the axial strain reaches about 35% in the compression simulation and 38% in the extension simulation, after which the deviatoric stress remains more or less constant, i.e., the critical state is attained. The attained strengths at the critical state are over 30 MPa. In

a real case, such a highly dilative response may be counteracted by the contractive trend due to grain crushing. This mechanism is not considered in the current study.

3.1.2 Cyclic loading simulations

Figure 4 presents the stress-strain responses of the loose sample subjected to cyclic constant-volume shearing. The excess pore water pressure is calculated as the difference between the mean effective stress at the initial state and that at the current state. The solid circles in Figure 4 mark the instants when flow deformation is triggered and are denoted as IFD i.e., the pore water pressure firstly approximates the initial mean effective stress or the axial strain firstly exceeds 5%. In some cases (i.e., q_{cyc} = 150 kPa and 300 kPa for the loose sample), although the axial strain has exceeded 5% axial strain, the effective stress is still decreasing. For these simulations, we took the instant when the minimal effective stress is reached as the onset of flow deformation. As Figures 4(b)-(c) show, following IFD, the axial strain develops sharply without an obvious change in the deviatoric stress, showing runaway-type deformation typical for loose sands. When $q_{cyc} \geq$ 180 kPa, flow deformation occurs in the compression side, while flow deformation occurs in the extension side when q_{cyc} = 150 kPa. This is because, as Figure 4(d) shows, the stress paths of the three simulations with $q_{cyc} \geq$ 180 kPa cross the ISL-C before intersecting the ISL-E whereas the stress path of the simulation with q_{cyc} = 150 kPa intersects the ISL-E before reaching the ISL-C. This supports the hypothesis of Yang and Sze [6] that the failure direction in cyclic flow liquefaction depends on the spatial relationship between the cyclic stress path and the monotonic flow liquefaction lines. As shown in the inset of Figure 4(d), the IDF states of the four simulations lie close to the zone bounded by the critical state line and the instability line, which is the failure zone defined by Hyodo et al.[3]. Note that the critical state line was determined based on Fig. 3(b) and some other supplemental drained simulations which are not shown for conciseness.

For the three simulations in C1, as Figure 5(a) shows, the excess pore water pressure increases gradually as the cyclic loading proceeds before reaching around the 12^{th}, 1.11^{th} and 0.54^{th} loading cycles for simulations with q_{cyc} = 200 kPa, 300 kPa and 400 kPa, respectively. At these instants (marked by solid diamonds) the excess pore water pressure jumps abruptly to a considerably large

value, after which the sample response changes from contractive to dilative, marking the phase transformation (PT) state in cyclic loading. Immediately after the PT state, the pore water pressure decreases due to dilation and then increases again due to contraction, momentarily reaching the mean effective stress at around the 12.5th, 1.52th and 1.01th loading cycles for simulations with q_{cyc} = 200 kPa, 300 kPa and 400 kPa, respectively. The change from the dilative to the contractive response is caused by the reversal of loading direction. These instants (the solid circles) are determined as the onset of flow deformation. This process is repeated in the following loading cycles and the axial strain is developed in a double-amplitude manner (Figure 5(b)). As Figure 5(c) shows, the axial strain increases substantially after the PT state. A butterfly-shape stress path is identified for the dense sample (Figure 5(d)). The double-amplitude axial strain and butterfly-shape stress path represents the typical features of cyclic mobility. Similar to the loose sample, the stress paths of the three simulations of C1 are bounded by the monotonic CSLs obtained in triaxial compression and triaxial extension simulations.

As noted by Idriss and Boulanger [25] and Sze [26] the relationship between the cyclic stress ratio (CSR) and the number of loading cycles to initial flow deformation (N_{IF}) can be represented by a power-law function,

$$CSR = mN_{IF}{}^{n} \tag{2}$$

in which m and n are fitting parameters. Figure 6 plots the CSR-N_{IF} relationship for the dataset presented in the current study. The data for Toyoura sand at the same initial confining pressure obtained in experiments conducted by Sze [26] are overlaid for comparison. The DEM simulation data can be well represented by Eq. 2 with the fitting parameters m = 0.3703 and n = -0.251for C1 simulations and m = 0.2237 and n = -0.148 for C2 simulations. The number of loading cycles to initial flow deformation increases as packing density increases. The CSR-N_{IF} relationship obtained in DEM simulations lies between the experimental data with a relative density D_r = 50% and that with a relative density of D_r = 25%.

3.2 Conditions of onset of flow failure

3.2.1 Hill's condition of instability

Hill [27] proposed using the second-order work d^2W (Eq. 3) to evaluate the stability of granular materials, i.e., a granular material is stable only when $d^2W > 0$.

$$d^2W = d\varepsilon_v dp' + d\varepsilon_q dq \tag{3}$$

in which $d\varepsilon_v$ and $d\varepsilon_q$ are respectively the volumetric strain and deviatoric strain increments. For the constant-volume simulations, Eq. 3 can be reduced to $d^2W = d\varepsilon_q dq$. Hill's condition of instability has been shown to be effective to describe the instability of sands subjected to constant shear stress loading conditions in both laboratory tests [28] and DEM simulations [29].

Figure 7(a) shows the evolution of d^2W for the loose sample subjected to triaxial compression. In accordance to Figure 2(a), the solid diamond marks the instability state. In order to clearly show the d^2W curve adjacent to the instability state, only the data within 0-2.0% axial strain are presented. d^2W surges to a peak value immediately after loading is commenced, after which d^2W drops rapidly and approaches zero at the instability state. After the instability state has been reached, the d^2W curve oscillates around the x axis, indicative of instability. The variation of d^2W during cyclic loading for the dense sample subjected to q_{cyc} =200 kPa is shown in Figure 7(b). d^2W is small and positive before reaching the phase transformation state (solid diamond). From the inset, it can be seen that d^2W oscillates slightly after the phase transformation state and becomes small and positive again until reaching the initial flow deformation instant (solid circle), after which d^2W oscillates quite significantly, indicating a highly instable state. d^2W becomes positive again after a short period of severe fluctuation. The procedure is repeated in the following loading cycles. Figure 7 clearly shows that Hill's condition of instability can also be used to evaluate the onset of flow failure for sands under both monotonic and cyclic undrained loading conditions.

3.2.2 Mechanical stability

Kruyt & Rothenburg [30] used an index of redundancy which is defined as the ratio of the total number of constraints at contacts to the total number of degrees of freedom to quantify the mechanical

redundancy within a discrete granular system. Here, mechanical redundancy means the total number of constraints provided by the contacts is larger than the total number of degrees of freedom within the system. For a three-dimensional problem, considering constraints on three translational motion directions for elastic contacts (at which $|f_t| < \mu f_n$, where f_t and f_n are the tangential and normal contact forces, respectively) and only one constraint along the normal direction for plastic contacts at which the sliding force limit is reached, i.e., $|f_t| = \mu f_n$. The total number of constraints provided by the contacts can be quantified as $3 \cdot (1-f) \cdot N_c + f \cdot N_c = (3-2f)N_c$, in which f is the sliding fraction and N_c is the total number of contacts. In total there are $6N_p$ degrees of freedom for a 3D system where N_p is the total number of particles and thus the index of redundancy I_R can be expressed as:

$$I_R = \frac{(3-2f)N_c}{6N_p} \tag{4}$$

If I_R is smaller than 1, the total number of constraints provided by the contacts will be smaller than the total number of degrees of freedom within the sample. In such cases, the particle may lose its stability and the sample may flow subjected to shearing. Kruyt & Rothenburg [30] proposed to substract the number of particles with zero contacts from N_p considering that these particles are unlikely to participate in force transmission. According to this principle, the corresponding index of redundancy I_R^{NR} becomes:

$$I_R^{NR} = \frac{(3-2f)N_c}{6(N_p - N_P^0)} \tag{5}$$

where N_P^0 denotes the number of floating particles (rattlers) with zero contacts. If I_R (I_R^{NR}) is greater than or equal to 1.0, the system is mechanically stable; otherwise, the system is mechanically unstable.

Figure 8 presents the variation of indexes of redundancy defined in Eq. (4) and Eq. (5) during monotonic compression shearing on the loose and the dense samples. The variations of indexes of redundancy during monotonic extension shearing are similar to Figure 8 and thus are not shown for conciseness. For the loose sample, as Figure 8(a) shows, I_R and I_R^{NR} show a similar trend, i.e., they are the largest after isotropic compression (I_R = 1.047, I_R^{NR} = 1.262), but drop abruptly at the initial stage of loading reaching the minimal values at about 2.5% axial strain (I_R = 0.232, I_R^{NR} = 0.614) which corresponds to the instant when the sample completely liquefies (see Figure 2(a)). Both I_R and I_R^{NR} recover thereafter and reach constant values at the critical state. For the dense sample, I_R =

1.086 and I_R^{NR}=1.293 at the beginning of shearing. I_R and I_R^{NR}initially drop slightly to a minimal value when the axial strain reaches 1%, and gradually increase thereafter until a constant value is approached at around 30% axial strain. For the loose sample, both I_R and I_R^{NR} are below 1.0 after liquefaction has occurred, indicating that it is in a mechanically unstable state. For the dense sample, I_R is below 1.0 between 0.5% axial strain and 6% axial strain, which according to the definition of I_R indicates that the dense sample should be in an unstable state during this loading period. This is contradictory to the stress-strain curves presented in Figure 3 which show that the dense sample behaves consistently dilative. For I_R^{NR} of the dense sample, it is consistently larger than 1.0 during the entire loading procedure, which agrees with the stress-strain curves shown in Figure 3.

Evolutions of indexes of redundancy during cyclic loading on the loose and dense samples are shown in Figure 9. For both the loose and the dense samples, evolutions of I_R and I_R^{NR} show a saw-type trend: both I_R and I_R^{NR} decrease at the start of each loading cycle and reach a local minimum value each time when the loading direction is reversed, i.e., when the number of loading cycles ($N=t/T$) equals to an odd number of times that of 1/4; immediately after reversal of the loading direction I_R and I_R^{NR} go up sharply to a local peak and decrease thereafter until the next valley point is reached. This procedure is repeated until initial flow deformation occurs. I_R and I_R^{NR} are overall in a decreasing trend. After initial flow deformation has been triggered, I_R and I_R^{NR} temporarily drops to very small values at each liquefaction instant but recover immediately and dramatically thereafter due to change of loading direction. As Figure 8 shows, I_R drops below 1.0 before the onset of flow deformation, while I_R^{NR} drops below 1.0 only at the instants when flow failure occurs. Therefore, I_R^{NR} defined excluding floating particles is a better index to evaluate the stability of granular materials subjected to both monotonic and cyclic loading conditions. This is sensible as I_R considers all the particles within a granular system while I_R^{NR} only reflects the stability of the force transmission network.

3.2.3 Structural anisotropy

The macro stress-strain behaviour of granular materials is related to the variation of the microstructures. Satake [31] proposed an expression of fabric tensor to describe the microstructure of a discrete granular system:

$$\Phi_{ij} = \frac{1}{N_c}\sum_{k=1}^{N_c} n_i^k n_j^k \ (k = 1,2,3) \tag{6}$$

where n_i^k denotes the unit contact normal component in the *i*th direction. The principal values of Eq. 6 quantify the clustering degree of contacts in each principal stress direction. In particular, the deviatoric fabric, $\Phi_d = \Phi_1 - \Phi_3$, i.e., the difference between the major (Φ_1) and minor (Φ_3) principal values of the fabric tensor, has been widely used to quantify the structural anisotropy of granular assemblies [32-34]. Wang et al. [19] used the difference between the principal values in the horizontal and vertical directions to quantify the internal structure change during cyclic loading.

Figure 10(a) shows the evolution of the three principal fabrics of the loose sample during monotonic loading. The intermediate (Φ_2) and minor (Φ_3) principal fabrics are close to each other as a $\sigma'_2 = \sigma'_3$ condition is prescribed in the servo control scheme while the major principal fabric (Φ_1) remains the largest throughout shearing. Φ_1 increases sharply while Φ_2 and Φ_3 experience a dramatic fall at about 1.5% axial strain. Similar to Φ_1, Φ_d also experiences a sudden jump prior to complete liquefaction. Wang et al. [19] also observed more severe change of fabric anisotropy after liquefaction. Figure 10 indicates that as the number of contacts within the system decreases due to complete liquefaction, the remaining contacts have to align more closely in the major principal stress direction to resist as much external loading as possible, which leads to the sharp increase in the structural anisotropy. It should be noted that the inflection points in Figures 10(a) and (b) appear before complete liquefaction, which indicates that the macro-scale responses lag the structural adjustment.

Evolutions of the three principal fabrics and the deviatoric fabric of the dense sample during monotonic compression loading are presented in Figure 11. The major principal fabric increases while the intermediate and minor principal fabrics decrease at the initial stage of loading. Φ_1 reaches

a peak value, while Φ_2 and Φ_3 attain a minimal value at about 10% axial strain, after which Φ_1 decreases and Φ_2 and Φ_3 increase until approximately constant values are reached respectively at the critical state. Φ_d increases initially as loading commences, reaching a peak value at about 10% axial strain, after which Φ_d decreases and tends to become almost constant after around 35% axial strain has been attained.

Evolution of structural fabrics of the loose sample during cyclic loading is shown in Figure 12. As Figure 12(a) shows, prior to initial flow deformation, evolution of principal fabrics within a loading cycle can be divided into four distinct stages: 1) from 0 to 1/4 of a loading cycle (compression loading), Φ_1 increases to a local peak point but Φ_2 and Φ_3 decrease to a local valley point at 1/4 of a loading cycle (loading direction is reversed from compression to extension); 2) from 1/4 to 1/2 of a loading cycle (compression unloading), Φ_1 decreases but Φ_2 and Φ_3 increase, and $\Phi_1 \approx \Phi_2 \approx \Phi_3$ at 1/2 of a loading cycle ($q = 0$); 3) from 1/2 to 3/4 of a loading cycle (extension loading), Φ_1 and Φ_2 increase to a local peak value but Φ_3 decreases to a local valley point at 3/4 of a loading cycle (loading direction is reversed from extension to compression); 4) from 3/4 of a loading cycle to one loading cycle (extension unloading), Φ_1 and Φ_2 decrease but Φ_3 increases, and $\Phi_1 \approx \Phi_2 \approx \Phi_3$ at the end of each loading cycle (q=0). These four stages are repeated until flow deformation occurs. After flow deformation has been triggered: when flow occurs at instants close to the onset of a loading cycle (0^{th}, 1^{st} , ….), Φ_1 rises almost vertically to a local peak value while Φ_2 and Φ_3 drop abruptly to a local minimal value; when flow happens close to half of a loading cycle, Φ_1 and Φ_2 increase almost vertically to a local peak value while Φ_3 drops abruptly to a local minimal value. Φ_1 always decreases and Φ_3 always increases between two neighbouring instants of flow deformation, while Φ_2 is close to Φ_3 during compression loading and extension unloading, and is similar to Φ_1 during compression unloading and extension loading.

The abrupt changes in principal fabrics mark remarkable changes in structural anisotropy. As Figure 12(b) shows, before reaching flow deformation, similar to the principal fabrics, evolution of the deviatoric fabric can also be characterized into four stages: 1) Φ_d increases during the first quarter of a loading cycle, reaching a local peak value at a quarter of a loading cycle (loading direction is reversed from compression to extension); 2) Φ_d drops thereafter and reaches a local minimal value at half of a

loading cycle ($q = 0$); 3) Φ_d increases again reaching a local peak at 3/4 of a loading cycle (loading direction is reversed from extension to compression); 4) Φ_d drops again from 3/4 of a loading cycle to the end of a loading cycle ($q = 0$). This procedure is repeated until flow deformation occurs. After flow deformation has been triggered, the deviatoric fabric jumps suddenly to a local peak and decreases thereafter, temporarily reaching a local minimal value at the next instant of flow failure. Evolutions of structural fabrics of the dense sample presented in Figure 13 are similar to those of the loose sample presented in Figure 12 and thus are not elucidated herein in detail. The more severe change in deviatoric fabric post liquefaction in comparison to that before liquefaction was also observed by Wang et al. [19].

As noted in Section 3.1, the dense sample behaves consistently dilatively during monotonic loading (see Figure 3), while it liquefies in a form of cyclic mobility when subjected to cyclic loading (see Figure 5). This may be due to the difference in structural fabric evolutions during monotonic and cyclic loading. As Figure 11 shows, evolution of structural fabric of the dense sample during monotonic loading is also monotonic, while evolution of structural fabric of the dense sample during cyclic loading shows a repeating decrease-and-increase trend. This kind of periodic change in structural fabric may likely yield 'fatigue' of the soil skeleton accumulating more plastic strain at the contacts, which finally leads flow deformation during cyclic loading.

Figure 14 presents the variation of deviatoric fabric Φ_d with time ratio t/T (time divided by the cyclic period) normalized by the number of loading cycles to initial flow (N_{IF}) at four critical loading instants: 1) $q = 0$, approached by loading extension (LE); 2) $q = 0$, approached from unloading compression (UC); 3) $q = q_{cyc}$, when loading direction is reversed from compression to extension; 4) $q = -q_{cyc}$, when loading direction is reversed from extension to compression. The sample is in an isotropic stress state at instants 1) and 2), and is close to its most anisotropic state at instants 3) and 4). For both the loose and the dense samples, the values of Φ_d at $q = 0$ are small and remain almost constant until $(t/T)/N_{IF}$ reaches a critical value (0.98 and 0.96 for the loose and the dense samples, respectively), after which Φ_d increases dramatically and jumps abruptly to a peak value at the onset of flow deformation ($(t/T)/N_{IF} = 1$). Figure 14 also shows that after the onset of flow deformation Φ_d experiences a steep jump each time when liquefaction takes place. Regarding Φ_d at $q = q_{cyc}$, it is

consistently larger than Φ_d at $q = 0$ before the onset of flow deformation. For the loose sample, Φ_d at $q = q_{cyc}$ is initially small but starts to increase when $(t/T)/N_{IF}$ reaches 0.36. After flow failure has occurred, Φ_d at $q = q_{cyc}$ is larger at the instants when loading direction is reversed from extension to compression than that at the instants when loading direction is reversed from compression to extension.

Evolution of Φ_d at $q = q_{cyc}$ between $(t/T)/N_{IF} = 0$ and 0.9 for the dense sample is enlarged in the inset of Figure 14(b). Three distinct stages can be identified:

Stage I: before $(t/T)/N_{IF}$ reaches 0.78, evolution of Φ_d at $q = q_{cyc}$ is saw-type. Within each loading cycle, Φ_d at the compression-to-extension transition instants is always larger than that at the extension-to-compression transition instants. Φ_d values at both transition instants show an overall increasing trend. At this stage, the micro structure is elastic.

Stage II: between $(t/T)/N_{IF} = 0.78$ and $(t/T)/N_{IF} = 1.0$ (initial flow failure), Φ_d at $q = q_{cyc}$ increases monotonically.

Stage III: after initial flow failure, the evolution of Φ_d returns to a saw-type. In contrast to Stage *I*, Φ_d at the compression-to-extension transition instants is smaller than that at the extension-to-compression transition instants.

The gradual increase of structural fabric at Stage *I* and Stage *II* may reflect the fatigue and degradation of the soil skeleton caused by periodic shearing with constant amplitude. Referring to Figure 14(a), Stage *II* and Stage *III* are also obvious for the loose sample; whereas Stage *I* is absent for the loose sample. The absence of an elastic stage for the loose sample accounts for its lower resistance to flow failure. Figure 14 also indicates that the structural anisotropy at the loading direction reversal states ($q = q_{cyc}$) experiences obvious change earlier than the structural anisotropy at $q = 0$ state does.

Discussion and Conclusions

DEM simulations were carried out to investigate the onset of initial flow failure of sands. These include two monotonic triaxial compression simulations, two monotonic triaxial extension simulations and

seven constant-volume cyclic loading simulations. The influences of initial packing density and cyclic deviatoric stress amplitude on the onset of flow failure were investigated. The link between monotonic and cyclic behaviour was explored. Both the flow-type failure typical for loose sands and the cyclic mobility typical for dense sands under undrained cyclic loading conditions were captured. For the loose sample, DEM simulation results support the experimental observations of Vaid & Chern [7] and Yang & Sze [5-6]. The cyclic loading responses were shown to be related to the monotonic responses. The onset of flow failure lies in the failure zone bounded by the critical state line and instability line determined from monotonic simulations. Failure occurs in the compression loading direction when the stress path of the cyclic loading intersects the stress path of monotonic compression prior to the stress path of monotonic extension, and vice versa. The number of loading cycles to failure decreases as the cyclic deviatoric stress increases. However, for the dense sample, despite its persistently dilative response during monotonic shearing, cyclic mobility is observed with the effective stress dropping temporarily to zero and the axial strain developing in a double-amplitude manner. This agrees with Yang and Sze [5] who show that even a Toyoura sand sample with a relative density as high as 70% may still liquefy in a form of cyclic mobility.

The second-order work proposed by Hill [27] is used to evaluate the stability of the sample. The second-order work drops to below zero when the sample becomes unstable under both monotonic and cyclic loading conditions. Thus, Hill's condition of instability can be viewed as the macro-scale condition for the onset of flow failure. Two indexes of redundancy were used to evaluate the mechanical stability during both monotonic and cyclic shearing for the loose and the dense samples. DEM data revealed that the index of redundancy I_R^{NR} excluding rattlers with zero contacts is a better indicator of the mechanical stability of a granular system than the index of redundancy including rattlers. Under both monotonic and cyclic loading conditions, I_R^{NR} was greater than 1.0 before the onset of flow failure but decreased to less than 1.0 after flow. Therefore, $I_R^{NR} < 1$ can be taken as the micro-scale condition for the onset of flow failure.

Analysis of structural fabric revealed that flow failure is characterized by an abrupt change in microstructures which leads to a highly anisotropic fabric. The periodic change of structural fabric during cyclic loading leads to 'fatigue' and degradation of the soil skeleton. This is characterized by

increasing structural anisotropy at instants of loading direction reversal, which may account for the observed macro-scale phenomenon that the dense sample liquefies during cyclic loading despite neither phase transformation state nor instability state being present during monotonic loading. Furthermore, when looking at the structural anisotropy at the isotropic stress state ($q = 0$) and that at the most anisotropic stress state ($q = q_{cyc}$) separately, it is observed that the former is consistently smaller than the latter before initial flow but a converse trend is observed after flow deformation. The structural anisotropy at the states of loading direction reversal experiences obvious change earlier than the structural anisotropy at isotropic stress state ($q = 0$).

Acknowledgement

This research was funded by the Natural Science Foundation of China (No. 51509186).

Notation

$\boldsymbol{CSR}$ Cyclic stress ratio

$\boldsymbol{D_r}$ Relative packing density

d^2W second-order work

$\boldsymbol{e_0}$ Initial void ratio

$\boldsymbol{f}$ Sliding fraction

$\boldsymbol{f_n}$ Normal contact force

$\boldsymbol{f_t}$ Shear/tangential contact force

$\boldsymbol{I_R}$ Index of redundancy

$\boldsymbol{I_R^{NR}}$ Index of redundancy excluding rattlers

$\boldsymbol{m,n}$ Fitting parameters of the CSR-N_{IL} relationship

$\boldsymbol{N}$ Number of loading cycles

$\boldsymbol{N_c}$ Total number of contacts

$\boldsymbol{N_{IF}}$ Number of loading cycles to flow failure

$\boldsymbol{N_p}$ Total number of particles

$\boldsymbol{p'}$ Mean effective stress

$\boldsymbol{q}$ Deviatoric stress

$\boldsymbol{q_{cyc}}$ Cyclic deviatoric stress

$\boldsymbol{t}$ Running time

$\boldsymbol{\mu}$ Inter-particle friction coefficient

$d\varepsilon_v$ volumetric strain increment

$d\varepsilon_q$ deviatoric strain increment

σ'_1 Major principal stress

σ'_3 Minor principal stress

$\sigma'_{3,0}$ Initial confining pressure

Φ_d Deviatoric fabric

Φ_{ij} Fabric tensor

$\Phi_{1,2,3}$ Major, intermediate, minor principal fabrics

ω Cyclic loading angular frequency

References

[1] Castro, G. (1975). Liquefaction and cyclic mobility of saturated sands. *Journal of Geotechnical Engineering Division ASCE,* 101(GT6), 551-569.

[2] Hyodo, M., Murata, H., Yasufuku, N. & Fujii, T. (1991). Undrained cyclic shear strength and residual shear strain of saturated sand by cyclic triaxial tests. *Soils and Foundations* 31(3), 60-76

[3] Hyodo, M., Tanimizu, H., Yasufuku, N. & Murata, H. (1994). Undrained cyclic and monotonic triaxial behaviour of saturated loose sand. *Soils and Foundations* 34(1), 19-32.

[4] Lade P.V. (1993). Initiation of static instability in the submarine Nerlerk berm. *Canadian Geotechnical Journal,* 30, 895-904.

[5] Yang J. & Sze. H.Y. (2011a). Cyclic behavior and resistance of saturated sand under no-symmetrical loading conditions. *Géotechnique,* 61(1), 59-73.

[6] Yang J. & Sze H.Y. (2011b). Cyclic strength of sand under sustained shear stress. *Journal of Geotechnical and Geoenvironmental Engineering,* 137(12), 1275-1285.

[7] Vaid, Y. P. & Chern, J. C. (1985). Cyclic and monotonic undrained response of sands. In *Advances in the art of testing soils under cyclic loading conditions* (ed. V. Khosla), pp. 171–176. Reston, VA: ASCE.

[8] Yang, J. (2002). Non-uniqueness of flow liquefaction line for loose sand. *Géotechnique,* 52(10), 757–760

[9] Alarcon-Guzman, A., Leonards, G. & Chameau, J.L. (1988) Undrained monotonic and cyclic strength of sands. *Journal of Geotechnical Engineering,* 114(10), 1089-1109.

[10] Andrade, J.E., Ramos, A.M. & Lizcano, A. (2013) Criterion for flow liquefaction instability. *Acta Geotechnica*, 8, 525–535

[11] Mital, U. & Andrade, J.E. (2016) Mechanics of origin of flow liquefaction instability under proportional strain triaxial compression. *Acta Geotechnica*, 11, 1015–1025

[12] Cundall, P.A., & Strack, O.D.L. (1979). A discrete numerical model for granular assemblies. *Géotechnique*, 29(1), 47–65.

[13] O'Sullivan, C. (2011). Particulate discrete element modelling: A geomechanics perspective (1st ed.). Oxford: Taylor & Francis.

[14] Ng, T.-T. & Dobry, R. (1994). Numerical simulations of monotonic and cyclic loading of granular soil. *Journal of Geotechnical Engineering*, 120(2), 388–403.

[15] Sitharam, T. G. (2003). Discrete element modelling of cyclic behaviour of granular materials. *Geotechnical and Geological Engineering*, 21(4), 297–329.

[16] Kuhn, M.R., Renken, H.E., Mixsell, A.D. & Kramer, S.L. (2014) Investigation of Cyclic Liquefaction with Discrete Element Simulations. *Journal of Geotechnical and Geoenvironmental Engineering*, 140(12), 1-13

[17] Xu, X.M., Ling, D.S., Cheng, Y.P. & Chen, Y.M. (2015) Correlation between liquefaction resistance and shear wave velocity of granular soils: a micromechanical perspective. *Géotechnique,* 65(5): 337-348

[18] Wang, G. & Wei, J.T. (2016) Microstructure evolution of granular soils in cyclic mobility and post-liquefaction process. *Granular Matter,* 18: 51 doi:10.1007/s10035-016-0621-5

[19] Wang R., Fu P., Zhang J.M. & Dafalias Y.F. (2016) DEM study of fabric features governing undrained post-liquefaction shear deformation of sand. *Acta Geotechnica*. 11 (6), 1321-1337.

[20] Itasca Consulting Group. Particle Flow Code in Three Dimensions: User's Manual, Version 4.0. Minneapolis, USA 2007.

[21] Simmons G. & Brace W.F. (1965). Comparison of static and dynamic measurements of compressibility of rocks. *Journal of Geophysical Research,* 70, 5649–5656.

[22] Bernhardt, M.L., Biscontin, G., O'Sullivan, C. (2016) Experimental validation study of 3D direct simple shear DEM simulations. *Soils and Foundations*, 56(3): 336-347

[23] Ishihara, K. (1993). Liquefaction and flow failure during earthquakes. *Géotechnique,* 43, No. 3, 351–415

[24] Lade, P. V. (1994). Instability and liquefaction of granular materials. *Computers and Geotechnics,* 16, No. 2, 123–151.

[25] Idriss, I.M., & Boulanger, R.W. (2006). Semi-empirical procedures for evaluating liquefaction potential during earthquakes. *Soil Dynamics and Earthquake Engineering,* 26, 115-130.

[26] Sze, H.Y. (2010). Initial shear and confining stress effects on cyclic behaviour and liquefaction resistance of sands. PhD thesis, The University of Hong Kong.

[27] Hill, R. (1958). A general theory of uniqueness and stability in elastic- plastic solids. *Journal of Mechanics and Physics of Solids*, 6(3), 236–249.

[28] Chu, J., Leong, W.K., Loke, W.L. & Wanatowski, D. (2012) Instability of loose sand under drained conditions. *Journal of Geotechnical and Geoenvironmental Engineering*, 138(2), 207-216

[29] Lopera Perez, J.C., O'Sullivan, C., Kwok, C.Y., Huang, X. & Hanley, K.J. (2016) Exploring the micro-mechanics of triaxial instability in granular materials. *Géotechnique*, 66(9),725-740

[30] Kruyt, N.P. & Rothenburg, L. (2009) Plasticity of Granular Materials: a Structural-mechanics View. *AIP Conference Proceedings*. 1073 (1), 1073–1076.

[31] Satake, M. (1982). Fabric tensor in granular materials. In P. A. Vermeer, & H. J. Luger(Eds.), IUTAM symposium on deformations and failure of granular materials (pp.63–68). Rotterdam: Balkema

[32] Thornton, C. (2000). Numerical simulations of deviatoric shear deformation of granular media. *Géotechnique,* 50(1), 43–53

[33] Huang, X., Hanley, K.J., O'Sullivan, C., Kwok, C.Y. & Wadee, M.A. (2014) DEM analysis of the influence of the intermediate stress ratio on the critical-state behaviour of granular materials. *Granular Matter*, 16(5): 641-655.

[34] Gu, X.Q., Huang, M.S., & Qian, J.G. (2014) DEM investigation on the evolution of microstructure in granular soils under shearing. *Granular Matter*, 16(1), 91-106

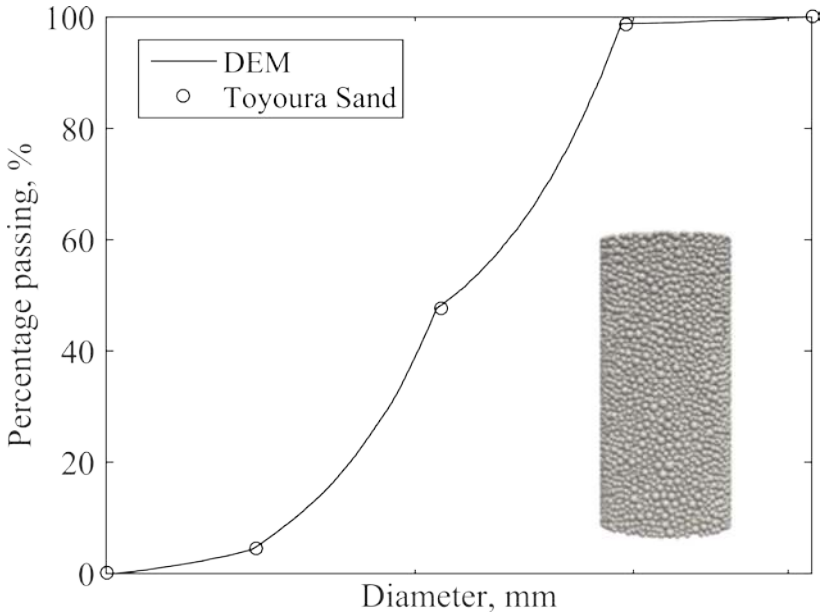

Fig. 1 Particle size distributions

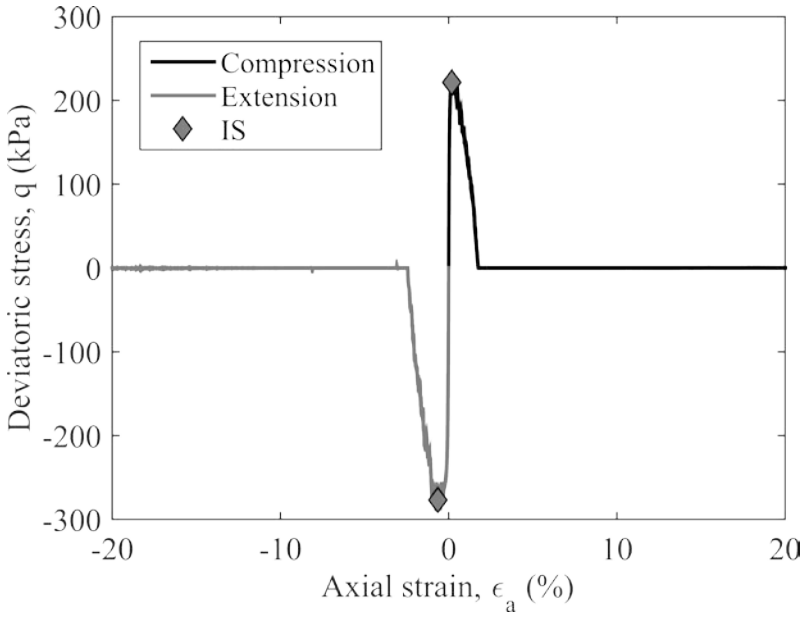

(a)

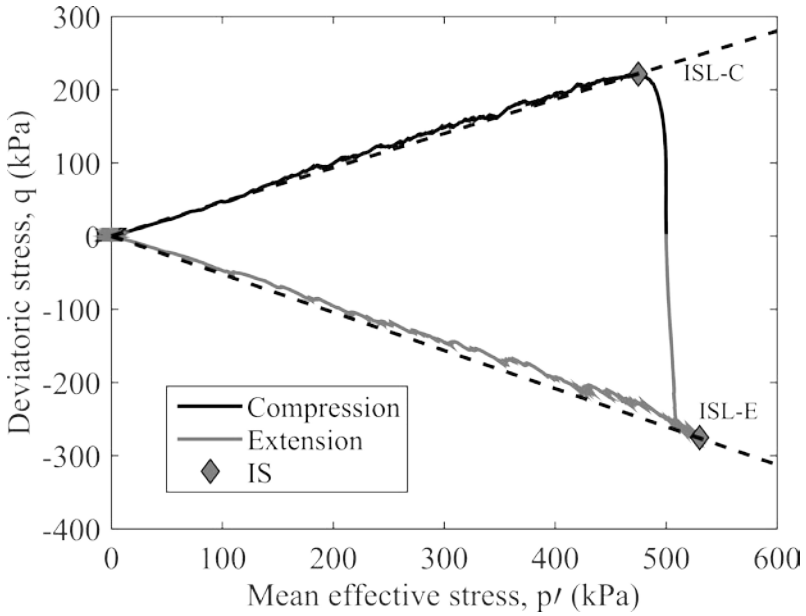

(b)

Fig. 2 Stress-strain responses of a loose sample subjected to monotonic undrained simulations (e_0 = 0.692, $\sigma'_{3,0}$ = 500 kPa): (a) Deviatoric stress vs axial strain; (b) stress path in *q-p'* space (ISL-C denotes instability line obtained from the monotonic triaxial compression simulation, ISL-E denotes instability line obtained from the monotonic triaxial extension simulation)

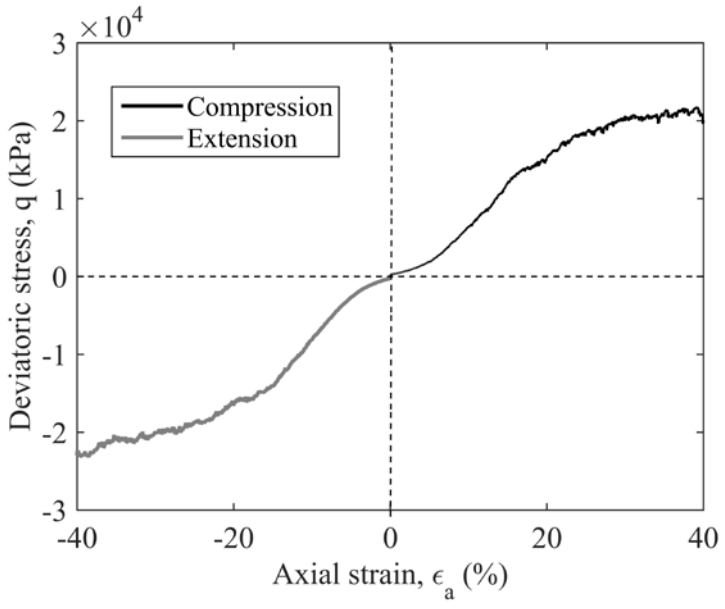

(a)

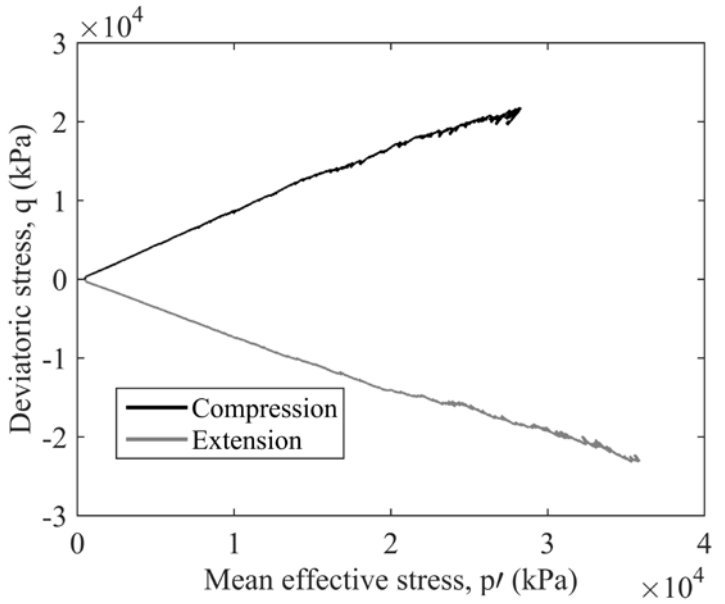

(b)

Fig. 3 Stress-strain responses of a dense sample subjected to monotonic undrained simulations (e_0 = 0.658, $\sigma'_{3,0}$ = 500 kPa): (a) Deviatoric stress vs axial strain; (b) stress path in *q-p'* space

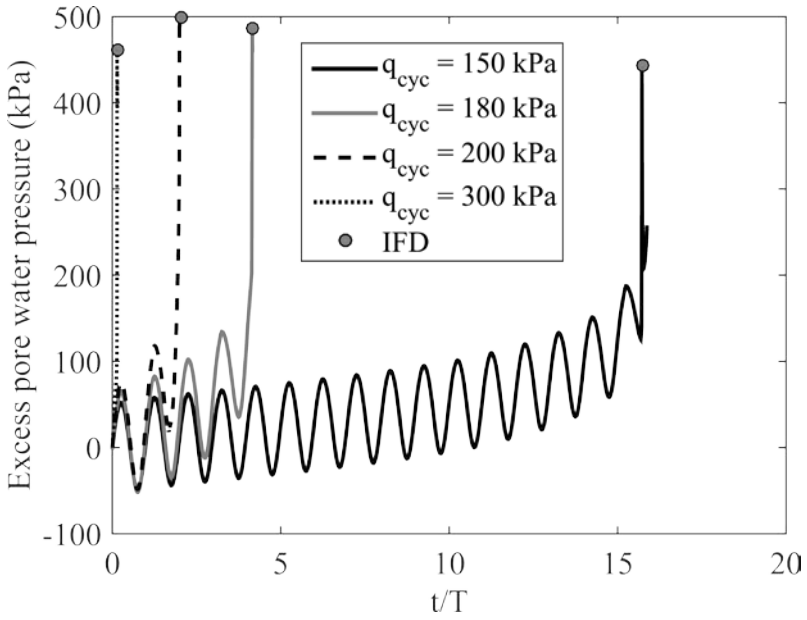

(a) Excess pore water pressure vs normalized time

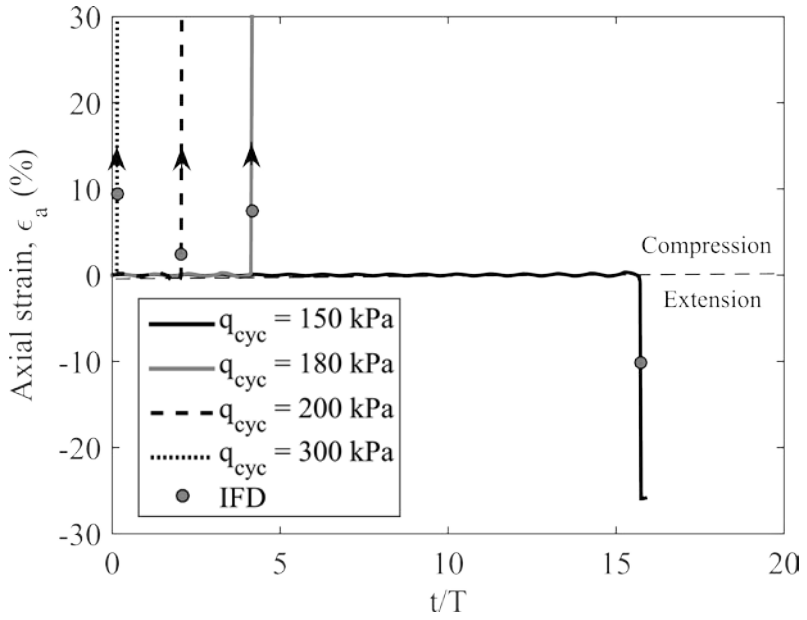

(b) Axial strain vs normalized time

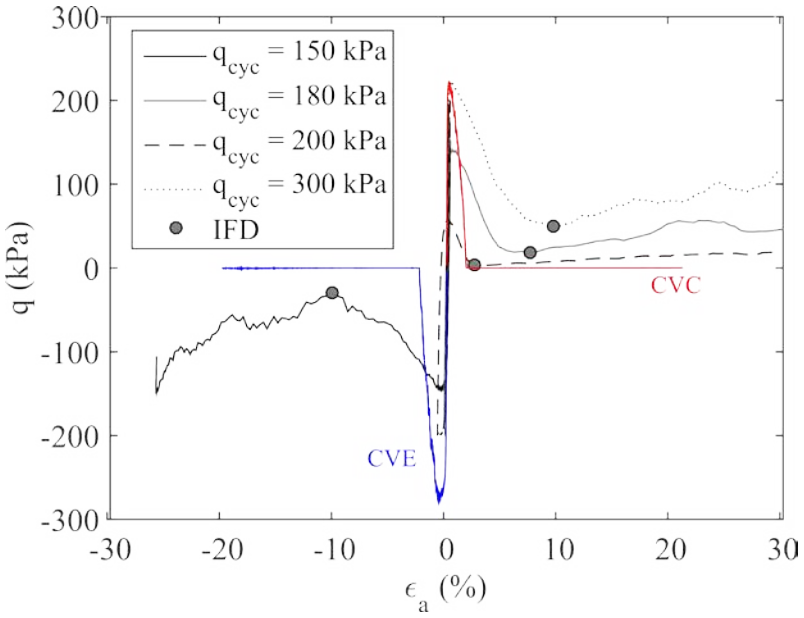

(c) Deviatoric stress vs Axial strain

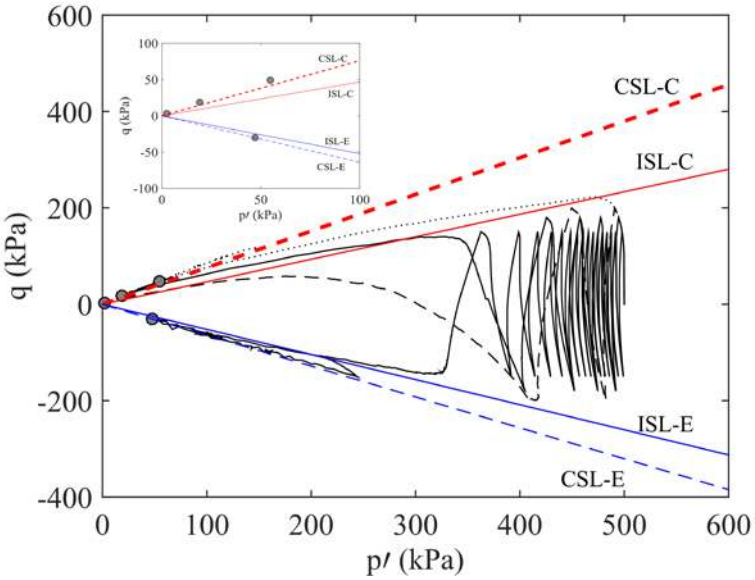

(d) *q-p'*

Fig. 4 Stress-strain responses of a loose sample subjected to cyclic undrained simulations (e_0 = 0.692, $\sigma'_{3,0}$ = 500 kPa; solid circles mark the onset of flow deformation; CVC and CVE indicate monotonic triaxial compression and monotonic triaxial extension, respectively; IFD denotes initiation of flow deformation; ISL denotes instability line; CSL-C and ISL-C are the critical state line and instability line obtained from triaxial compression simulation; CSL-E and ISL-E are the critical state line and instability line obtained from triaxial extension simulation)

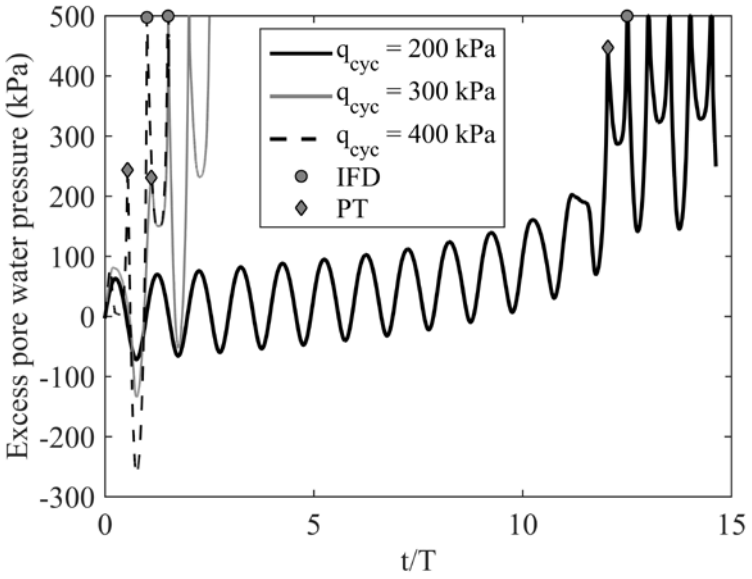

(a) Excess pore water pressure vs number of loading cycles

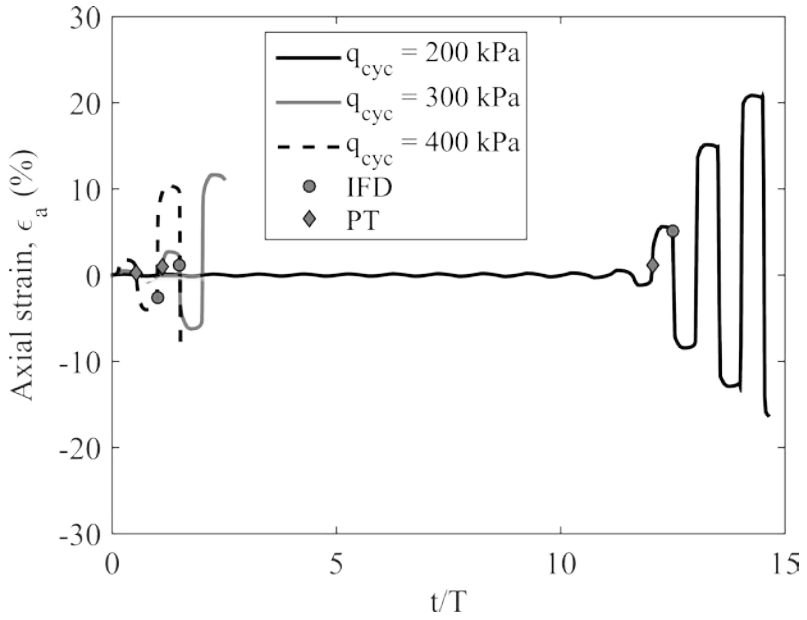

(b) Axial strain vs number of loading cycles

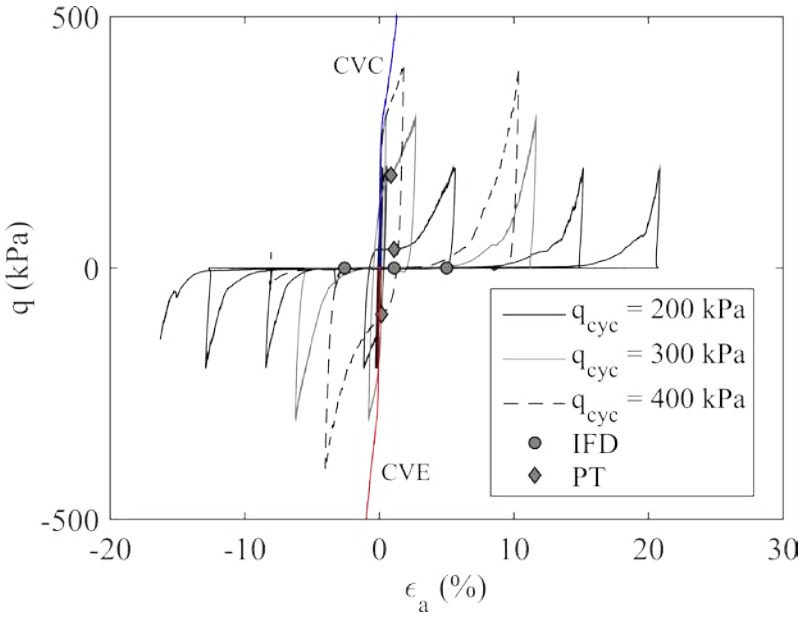

(c) Deviatoric stress vs Axial strain

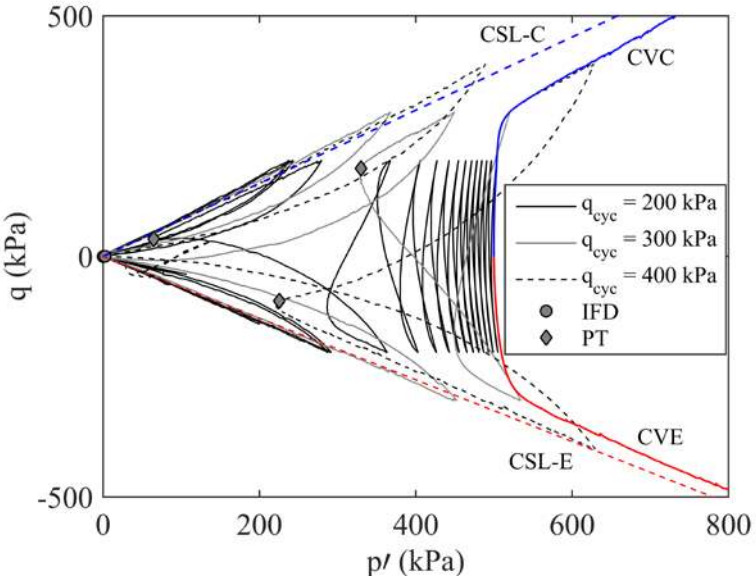

(d) *q-p'*

Fig. 5 Stress-strain responses of dense sample subjected to cyclic undrained simulation (e_0 = 0.658, $\sigma'_{3,0}$ = 500 kPa, solid diamonds show the phase transformation (PT) state, while solid circles mark the onset of flow deformation (IFD) ; CVC and CVE denote the constant-volume triaxial compression and constant-volume triaxial extension simulations, respectively; CSL-C and CSL-E are the critical state lines obtained in triaxial compression and triaxial extension simulations, respectively)

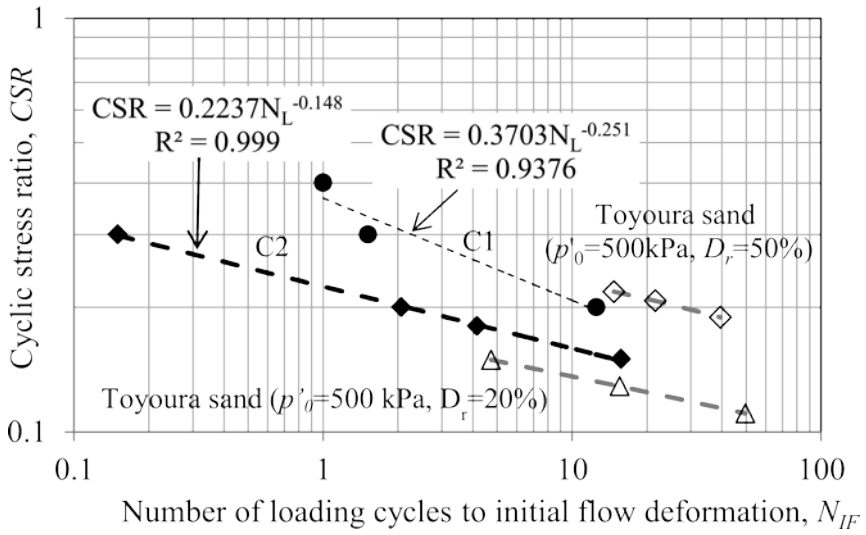

Fig. 6 Cyclic stress ratio against the number of loading cycles to initial flow deformation (Solid symbols are DEM simulation data, while hollow symbols are experimental data of Toyoura sand digitised from Sze (2010))

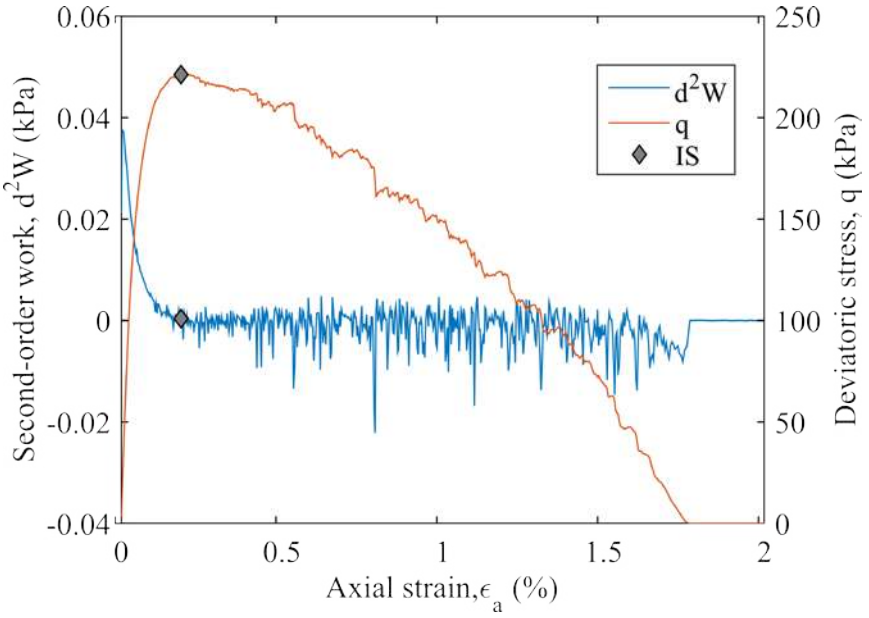

(a)

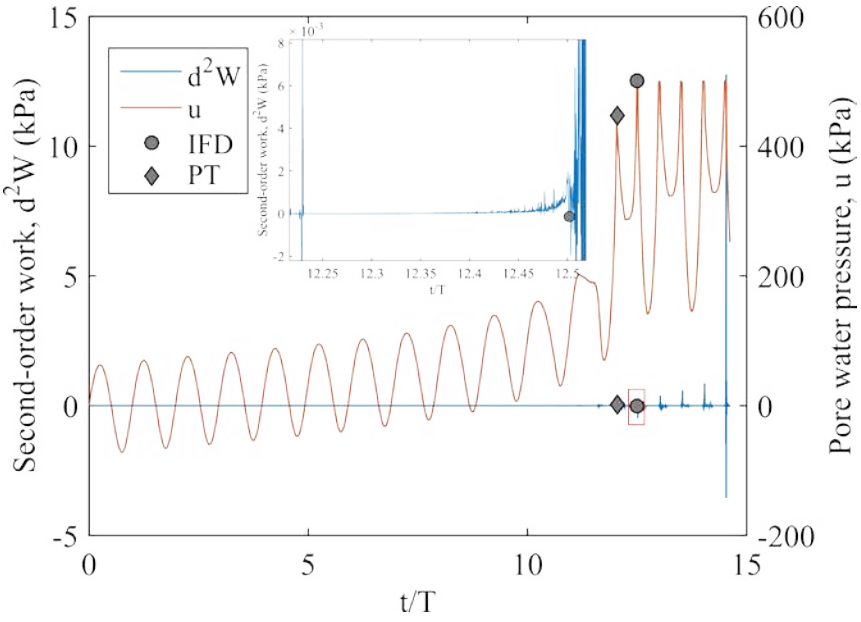

(b)

Figure 7 Evolutions of second-order work: (a) monotonic compression simulation for the loose sample; (b) cyclic loading simulation for the dense sample subjected to q_{cyc} = 200 kPa

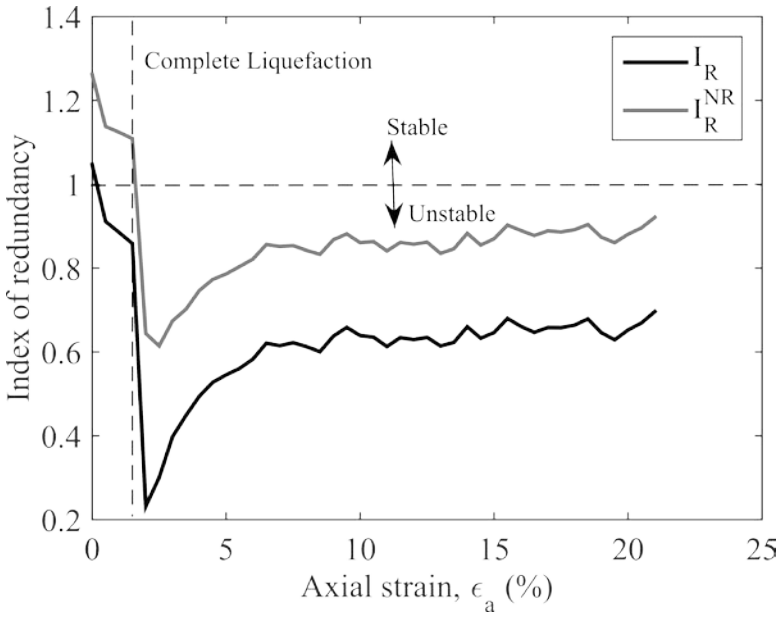

(a) loose sample (e_0 = 0.692, $\sigma'_{3,0}$ = 500 kPa)

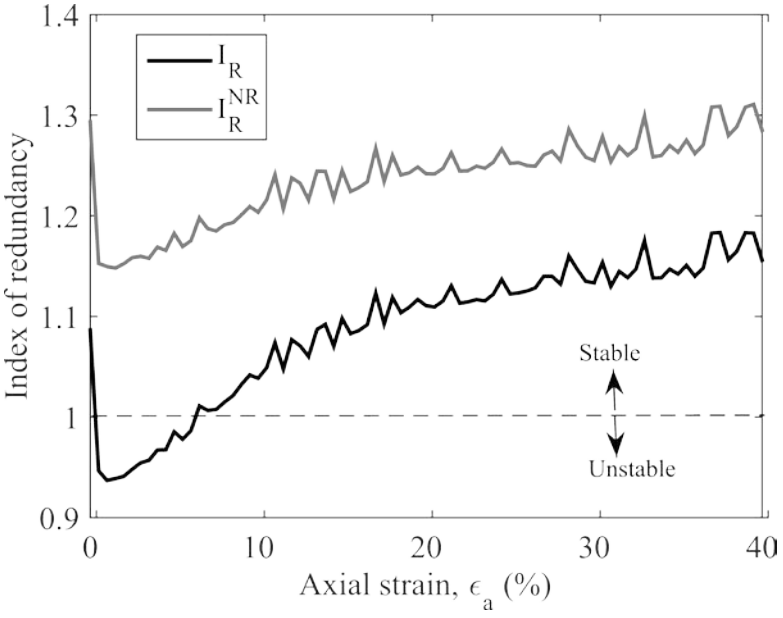

(b) dense sample (e_0 = 0.658, $\sigma'_{3,0}$ = 500 kPa)

Figure 8 Evolution of indexes of redundancy during monotonic compression triaxial loading simulations

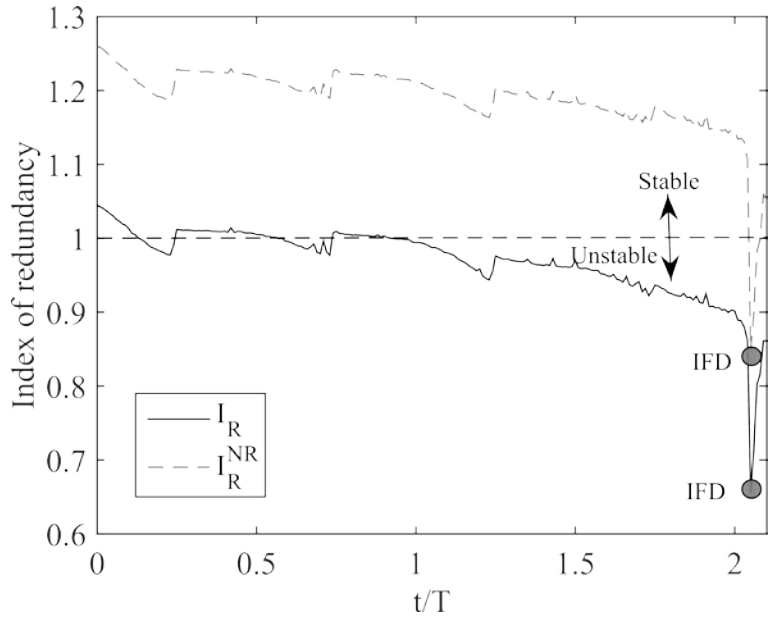

(a) loose sample (e_0 = 0.692, $\sigma'_{3,0}$ = 500 kPa, q_{cyc} = 200 kPa)

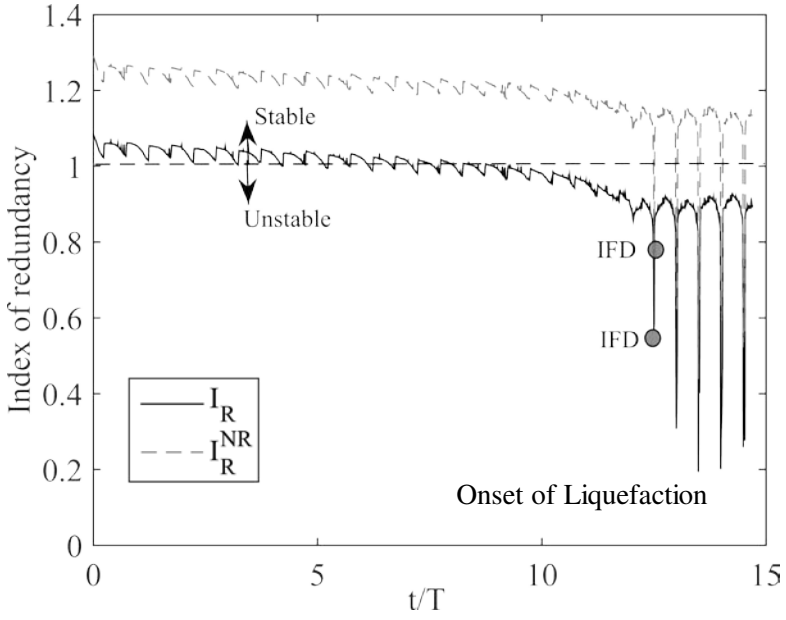

(b) dense sample (e_0 = 0.658, $\sigma'_{3,0}$ = 500 kPa, q_{cyc} = 200 kPa)

Figure 9 Evolution of indexes of redundancy during cyclic triaxial loading simulations

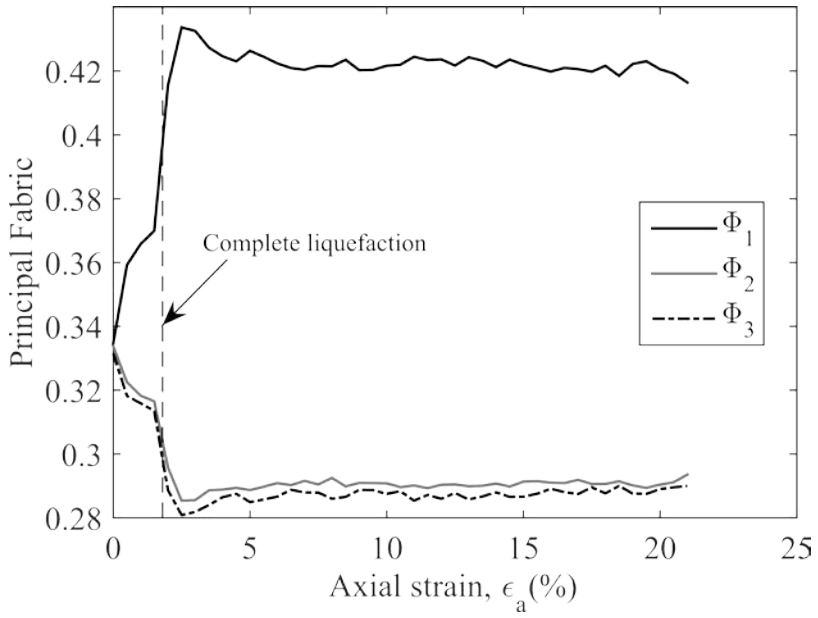

(a) principal fabrics

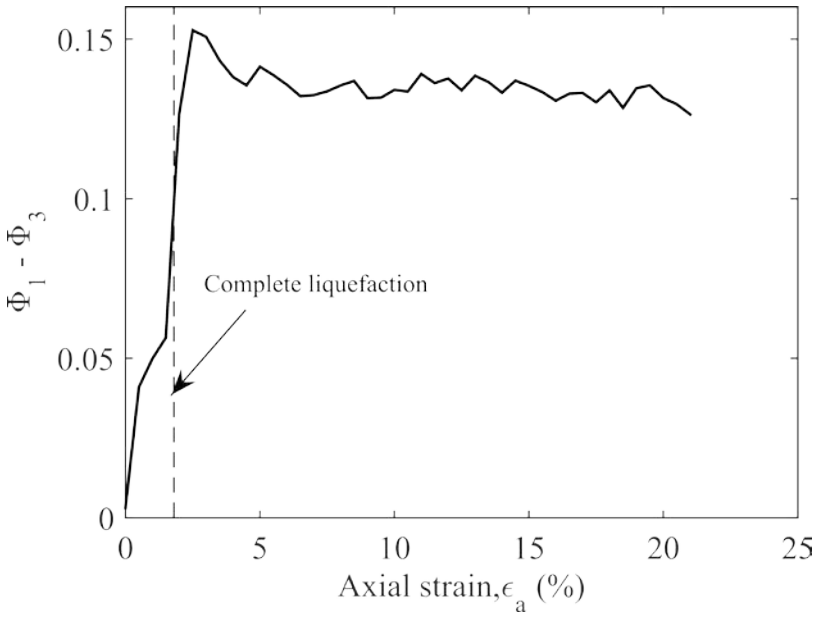

(b) deviatoric fabric

Figure 10 Evolution of structural fabric of the loose sample (e_0 = 0.692, $\sigma'_{3,0}$ = 500 kPa) during monotonic compression triaxial loading simulations

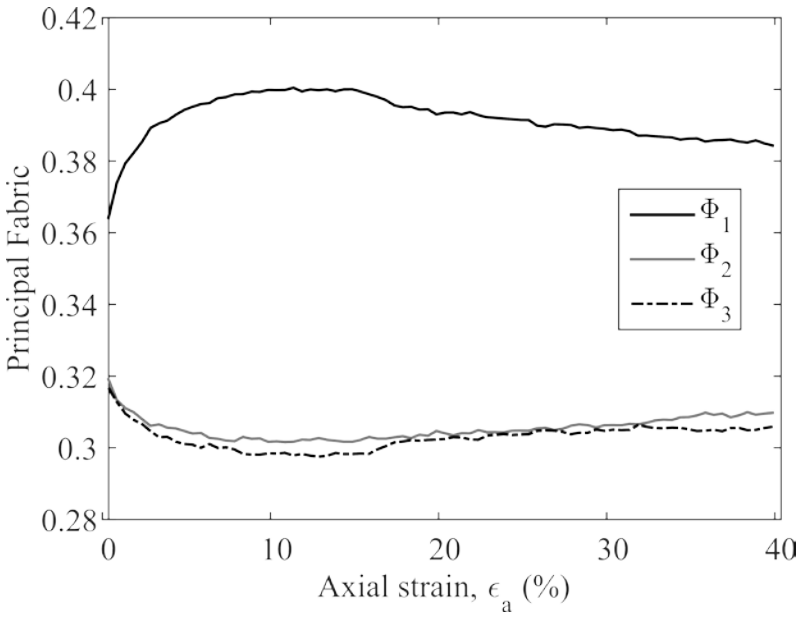

(a) principal fabrics

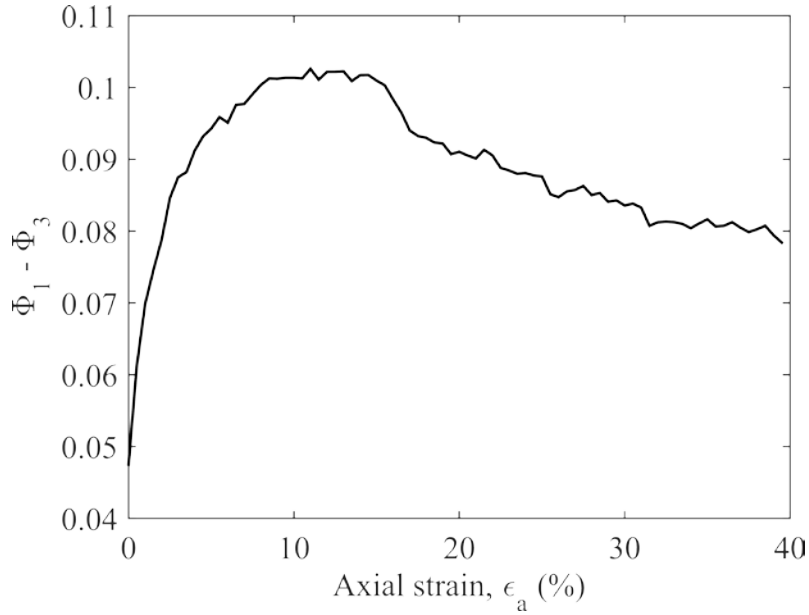

(b) deviatoric fabric

Figure 11 Evolution of structural fabric of the dense sample (e_0 = 0.658, $\sigma'_{3,0}$ = 500 kPa) during monotonic compression triaxial loading simulations

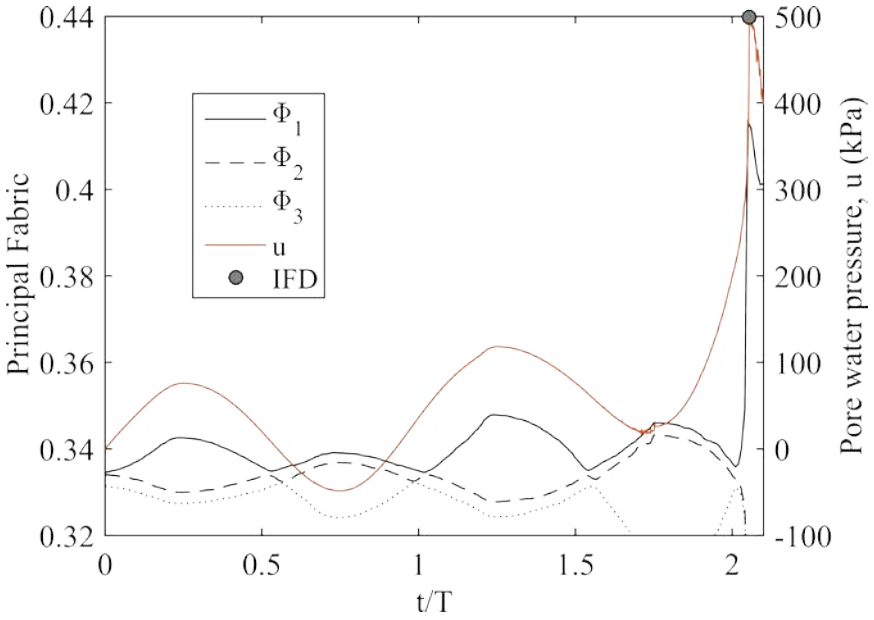

(a) principal fabrics

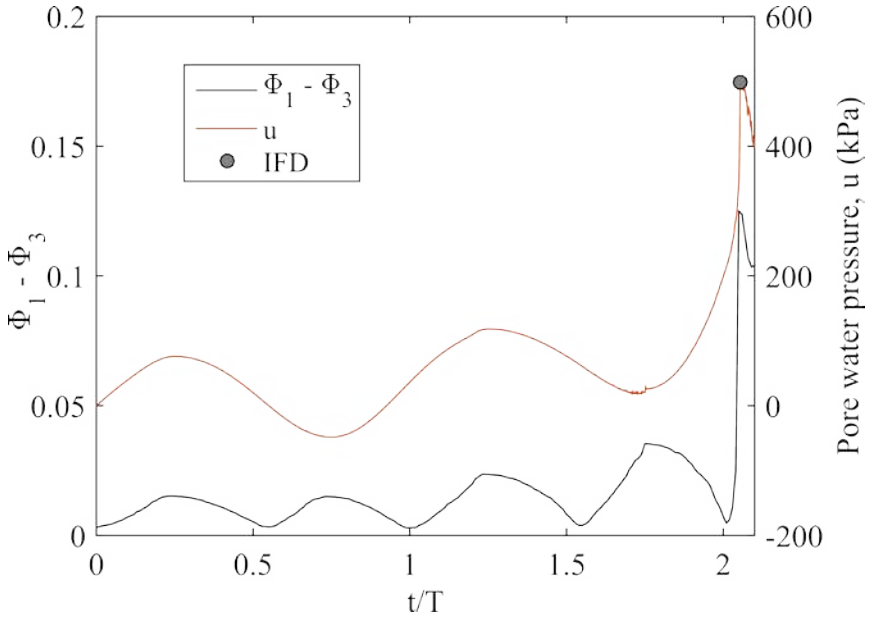

(b) deviatoric fabric

Figure 12 Evolution of structural fabric of loose sample (e_0 = 0.692, $\sigma'_{3,0}$ = 500 kPa, q_{cyc} = 200 kPa) during cyclic triaxial loading simulations

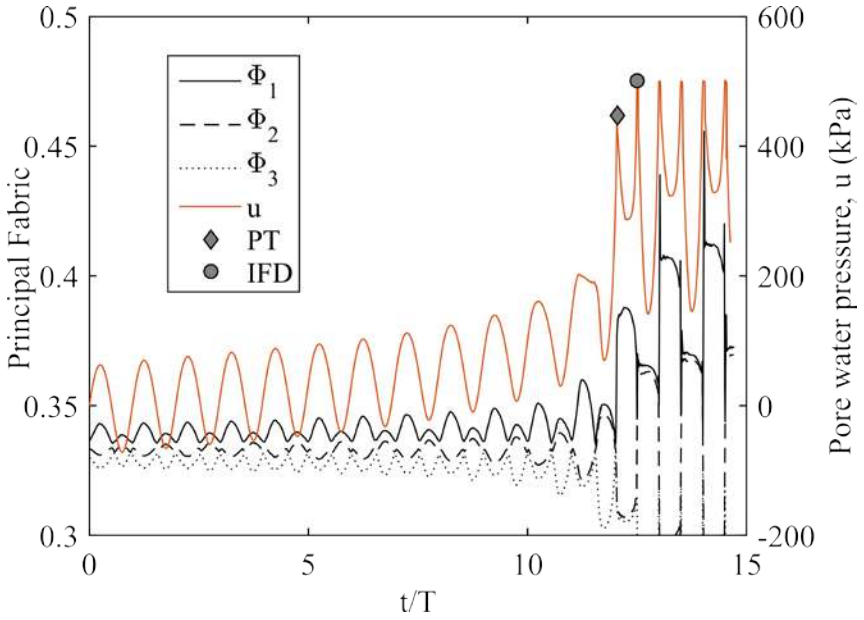

(a) principal fabrics

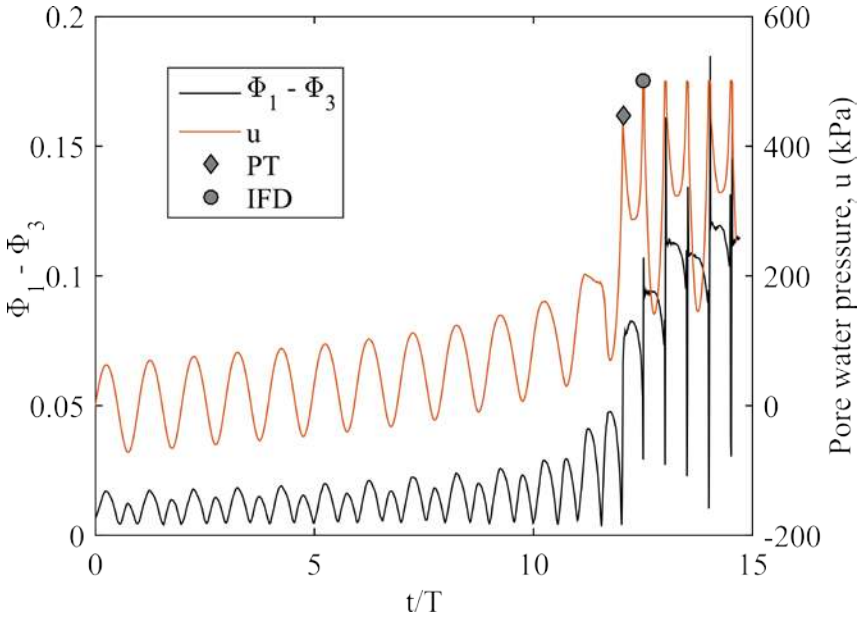

(b) deviatoric fabric

Figure 13 Evolution of structural fabric of dense sample (e_0 = 0.658, $\sigma'_{3,0}$ = 500 kPa, q_{cyc} = 200 kPa) during cyclic triaxial loading simulations

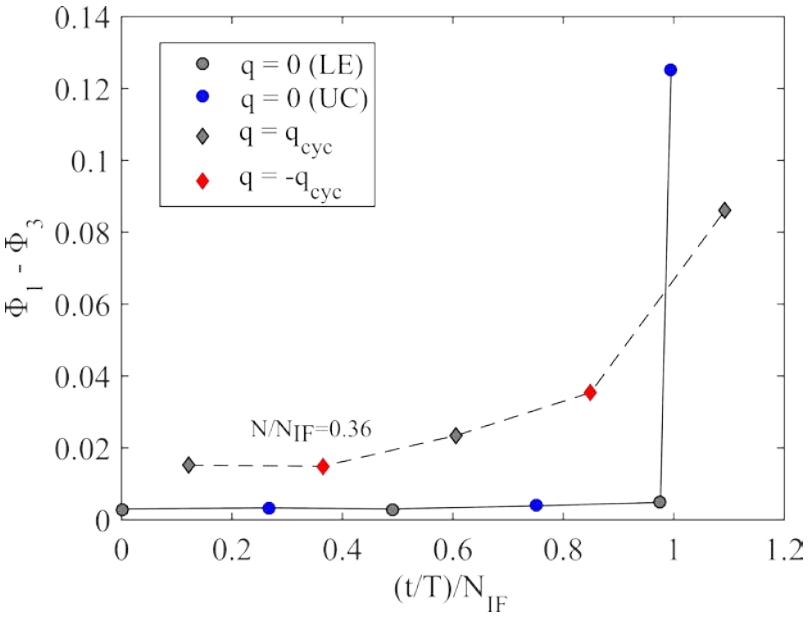

(a) loose sample (e_0 = 0.692, $\sigma'_{3,0}$ = 500 kPa, q_{cyc} = 200 kPa)

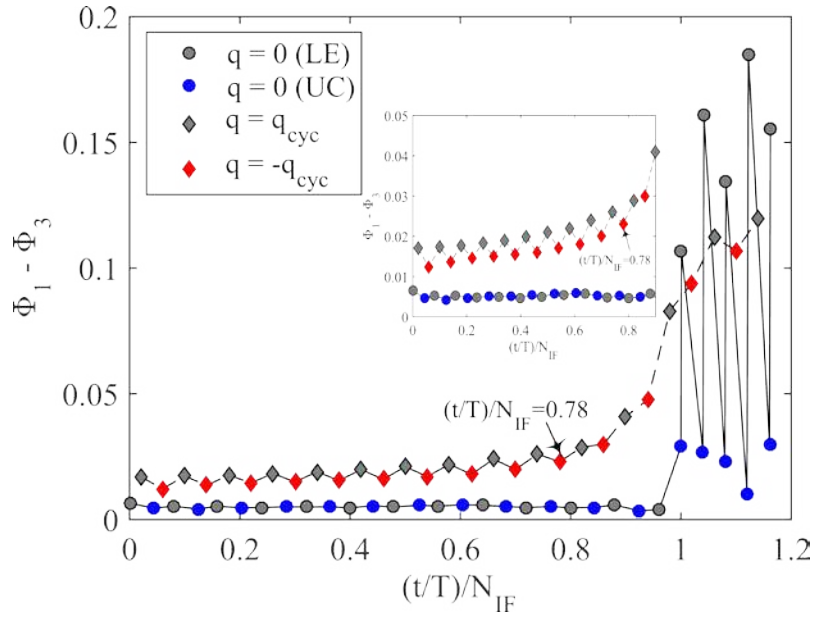

(b) dense sample (e_0 = 0.658, $\sigma'_{3,0}$ = 500 kPa, q_{cyc} = 200 kPa)

Figure 14 Structural anisotropy at selected characteristic instants (LE means loading extension; UC indicates unloading compression)